



# PCCP

## Electrochemical Flow Cell Enabling Operando Probing of Electrocatalyst Surfaces By X-Ray Spectroscopy and Diffraction

Journal:	<i>Physical Chemistry Chemical Physics</i>
Manuscript ID	CP-ART-12-2018-007423.R1
Article Type:	Paper
Date Submitted by the Author:	09-Feb-2019
Complete List of Authors:	<p>Farmand, Maryam; E O Lawrence Berkeley National Laboratory, Chemical Sciences Division  Landers, Alan; Stanford University, Department of Chemistry  Lin, John; Stanford University, Chemical Engineering  Feaster, Jeremy; Stanford University, Chemical Engineering  Beeman, Jeffrey; Lawrence Berkeley National Laboratory, Chemical Sciences Division; E O Lawrence Berkeley National Laboratory,  Ye, Yifan; Lawrence Berkeley National Laboratory, Advanced Light Source  Clark, Ezra; University of California Berkeley, Chemical &amp; Biomolecular Engineering  Higgins, Drew; University of Waterloo, Chemical Engineering  Yano, Junko ; Lawrence Berkeley National Lab., Physical Biosciences Division  Davis, Ryan; Univ. Stanford, SSRL  Mehta, Apurva; Univ. Stanford, SSRL  Jaramillo, Thomas; Stanford University, Assistant Professor of Chemical Engineering  Hahn, Christopher; Stanford University, Chemical Engineering; SLAC National Accelerator Laboratory, SUNCAT Center for Interface Science and Catalysis  Drisdell, Walter; Lawrence Berkeley National Laboratory, Materials Science</p>

**Electrochemical Flow Cell Enabling *Operando* Probing of Electrocatalyst Surfaces  
By X-Ray Spectroscopy and Diffraction**

Maryam Farmand<sup>1,2†</sup>, Alan T. Landers<sup>3,4†</sup>, John C. Lin<sup>4,5</sup>, Jeremy T. Feaster<sup>4,5,6</sup>, Jeffrey W. Beeman<sup>1</sup>, Yifan Ye<sup>1,2</sup>, Ezra L. Clark<sup>7</sup>, Drew Higgins<sup>4,5</sup>, Junko Yano<sup>8</sup>, Ryan C. Davis<sup>9\*</sup>, Apurva Mehta<sup>9\*</sup>, Thomas F. Jaramillo<sup>4,5\*</sup>, Christopher Hahn<sup>4,5\*</sup>, Walter S. Drisdell<sup>1,2\*</sup>

<sup>1</sup>Joint Center for Artificial Photosynthesis, Lawrence Berkeley National Laboratory, Berkeley, CA 94720, USA

<sup>2</sup>Chemical Sciences Division, Lawrence Berkeley National Laboratory, Berkeley, CA 94720, USA

<sup>3</sup>Department of Chemistry, Stanford University, Stanford, CA 94305, USA

<sup>4</sup>SUNCAT Center for Interface Science and Catalysis, SLAC National Accelerator Laboratory, Menlo Park, CA 94025, USA

<sup>5</sup>Department of Chemical Engineering, Stanford University, Stanford, CA 94305, USA

<sup>6</sup>Materials Science Division, Lawrence Livermore National Laboratory, Livermore, CA 94550, USA

<sup>7</sup>Chemical and Biomolecular Engineering Department, University of California Berkeley, Berkeley, CA 94720, USA

<sup>8</sup>Molecular Biophysics and Integrated Bioimaging Division, Lawrence Berkeley National Laboratory, Berkeley, CA 94720, USA

<sup>9</sup>Stanford Synchrotron Radiation Lightsource, SLAC National Accelerator Laboratory, Menlo Park, CA 94025, USA

†These authors contributed equally to this work.

## Abstract

The rational improvement of current and developing electrochemical technologies requires atomistic understanding of electrode-electrolyte interfaces. However, examining these interfaces under *operando* conditions, where performance is typically evaluated and benchmarked, remains challenging, as it necessitates incorporating an *operando* probe during full electrochemical operation. In this study, we describe a custom electrochemical flow cell that enables near-surface-sensitive *operando* investigation of planar thin-film catalysts at significant hydrogen evolution reaction (HER) rates (in excess of  $-100 \text{ mA/cm}^2$ ) using grazing incidence X-ray methods. Grazing-incidence X-ray spectroscopy and diffraction were implemented on the same sample under identical HER conditions, demonstrating how the combined measurements track changing redox chemistry and structure of Cu thin-film catalyst surfaces as a function of electrochemical conditions. The coupling of these methods with improved mass transport and hydrodynamic control establishes a new paradigm for *operando* measurement design, enabling unique insights into the key fundamental processes occurring at the catalyst-electrolyte interface.

## Introduction

Electrode-electrolyte interfaces play a critical role in both established and nascent electrochemical energy storage and conversion technologies, including Li ion batteries,<sup>1</sup> fuel cells,<sup>2</sup> and solar fuels generation. Hence, obtaining a molecular-scale understanding of the fundamental processes occurring at these interfaces is crucial to the rational design of electrodes and electrolytes for these applications. Characterizing these interfaces *in situ* remains challenging, as they may feature complex morphologies, compositions, and

dynamic behavior over various time scales, that make it difficult to deconvolute the signal produced at the interface from that of the bulk electrode or electrolyte.

For catalysis, *in situ* and *operando* studies have generally utilized two different approaches to probe electrode-electrolyte interfaces. The first is to apply traditional surface science or imaging methods to electrocatalysis. Some examples include sum frequency generation (SFG) spectroscopy, electrochemical scanning tunneling microscopy (EC-STM), attenuated total reflectance infra-red spectroscopy (ATR-IR),<sup>9-13</sup> transmission electron microscopy (TEM), ambient pressure X-ray photoelectron spectroscopy (APXPS),<sup>15-17</sup> and crystal truncation rod (CTR) scattering.<sup>18-20</sup> These methods are well suited to probe fundamental processes at the electrode-electrolyte interface, but often require strict experimental constraints such as low operating pressures, thin ( $\mu\text{m}$  or  $\text{nm}$  scale) liquid layers, and/or low to negligible current densities.<sup>5, 16, 21</sup> These constraints make it more challenging to relate fundamental understanding to the reaction conditions where the performance of a catalyst is typically assessed by measuring the intrinsic reaction rates. The second approach is to adapt techniques traditionally considered to be bulk-sensitive to study electrode-electrolyte interfaces. Synchrotron X-ray methods such as X-ray absorption spectroscopy (XAS) and X-ray diffraction (XRD) are widely used for *in situ* electrochemical studies, as the ability to penetrate through liquids and provide element-specific electronic and atomic structure information is ideal for characterizing electrode-electrolyte interfaces.<sup>18, 19, 22-24</sup> These measurements often employ nanostructured catalysts with high surface area to volume ratios to generate sufficient signal from the interface.<sup>24, 25</sup> However, the cell designs used

in these experiments can limit the achievable current densities to less than 1 mA/cm<sup>2</sup>.<sup>18, 19, 23</sup>

Regardless of the approach, bubbles formed from gaseous product evolution and/or poor mass transport of reactants to the surface can limit the range of applied electrode potentials where the catalyst can be evaluated, oftentimes restricting the range of measured current densities to undesirable values.<sup>22, 26-28</sup> Controlling mass transport is particularly important when evaluating the intrinsic kinetics of commonly studied electrocatalytic reactions such as CO<sub>2</sub> and O<sub>2</sub> reduction, where the low solubility of reactants can limit mass transport to the catalyst surface. Taken together, the aforementioned factors provide strong motivations to develop new *operando* methods for electrocatalysis, where the intrinsic reaction rates and the electrode-electrolyte interface can be simultaneously probed to yield fundamental understanding on how to improve catalytic performance. To this end, it is imperative that there is synergy between the design of the electrochemical cell and the implementation of the probe technique.

Herein, we detail the development and implementation of an *operando* electrochemical flow cell that enables probing of the catalyst-electrolyte interface using synchrotron grazing-incidence X-ray methods, at hydrogen evolution reaction (HER) rates that meet or exceed those typically used for evaluation and benchmarking.<sup>29</sup> The grazing-incidence geometry enables *operando* measurements of the dynamics of the near-surface region (~2-5 nm region from the surface into the bulk) of planar thin-film catalysts. The electrolyte flow regulates the hydrodynamics of the cell, allowing for H<sub>2</sub> bubbles to be easily removed from the surface while simultaneously controlling mass transport and the boundary layer thickness. We show that this control over the cell

hydrodynamics enables the collection of high-quality grazing-incidence X-ray diffraction (GIXRD) and grazing-incidence XAS (GIXAS) data at geometric current densities exceeding  $-100 \text{ mA/cm}^2$  on a planar Cu catalyst. Cu was chosen because it can have multiple oxidation states that are distinguishable by XAS and its K-edge energy is high enough to penetrate liquid layers on the order of mm thickness, but the cell can accommodate any smooth catalyst material with an accessible X-ray absorption edge. Combining both GIXRD and GIXAS allows probing of the local atomic arrangement near the catalyst surface, as well as the phase chemistry, lattice strain and morphology of the surface under identical reaction conditions. Using this combination of near surface-sensitive probes and reaction rates to examine the oxidation and reduction of planar Cu catalysts, we demonstrate that unique fundamental insights can be gained on the structural dynamics of catalysts under *operando* conditions.

### Measurement design

A custom 3D-printed electrochemical cell (3D printing by Protocafe) was designed and implemented to meet the aforementioned experimental requirements (Figure 1). Below, we briefly describe the important characteristics of the electrochemical flow cell; comprehensive details about the cell assembly process can be found within the Experimental section. The cell is designed for thin-film working electrode samples 3 mm by 10 mm; the 3 mm width allows the incident X-ray beam to pass through the cell at grazing angles (as low as  $0.1^\circ$ ) without prohibitive attenuation from liquid scatter. Two 50  $\mu\text{m}$  diameter Pt wires (Alfa Aesar, 99.99%) serve as the counter electrode and are mounted at a height of  $\sim 200 \mu\text{m}$  above the working electrode.

This parallel electrode geometry maintains consistent polarization across the working electrode, while still allowing fluoresced and diffracted X-rays to exit the cell between the wires. The reference electrode intersects the electrolyte inlet channel at a port near the working electrode, enabling operation in a three electrode configuration to accurately control the working electrode potential. The  $< 500 \mu\text{m}$  channel between the working and counter electrodes is open on the sides to allow X-rays to enter; polyimide film (Kapton) stretched over the top and sides of the cell and epoxy provide a robust seal for electrolyte flow, while also maintaining high transmissivity for X-ray measurements. Electrolyte flow through the channel enables control of the cell hydrodynamics, allowing for improved mass transport of reactant species. Additionally, electrolyte flow mitigates growth of bubbles from gaseous product evolution. This not only allows for the collection of high-quality X-ray measurements as shown below but also improves the stability of the current density measurements by preventing active sites from being blocked.

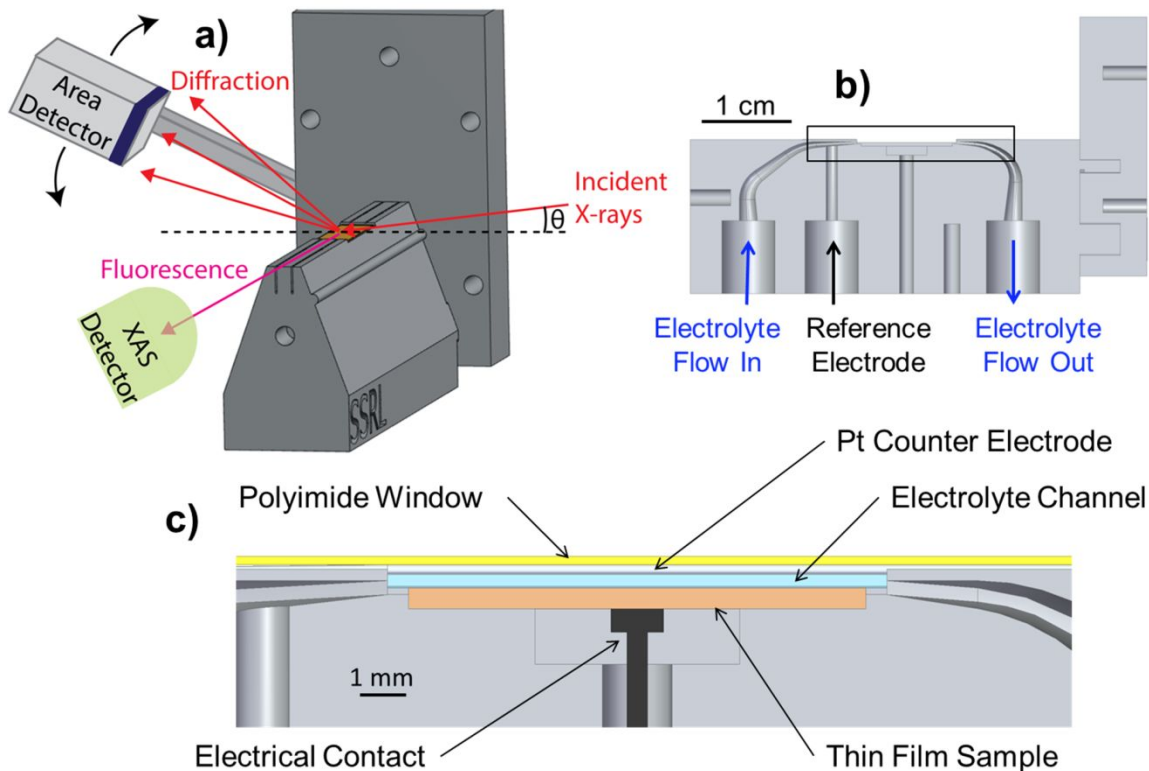


**Figure 1:** Electrochemical flow cell design. a) Schematic illustrating the experimental geometry for grazing incident, diffracted, and fluorescent X-rays. Not to scale; the cell is enlarged and the polyimide window is excluded for clarity. b) Side-view cross section of the electrochemical cell, showing the electrolyte flow channels and reference electrode port. c) Enlarged view of the indicated area in b). X-rays enter into the page, between the thin film sample and Pt counter electrode. Note that the polyimide window also seals the sides of the electrolyte channel where the X-rays enter.

To quantitatively demonstrate the effect of electrolyte flow rate on mass transport, we used potassium ferricyanide reduction on Au thin-film electrodes to calculate the boundary layer thickness as a function of electrolyte flow rate. Cyclic voltammograms show a clear increase in ferricyanide reduction current as the electrolyte flow rate increases (Figure 2a). Based on these voltammograms, we applied a potential of 0 V vs. RHE to the electrode to measure the steady-state current density in a region where ferricyanide reduction is diffusion limited (Figure 2b). From these measurements, we

calculated the boundary layer thickness (Figure 2c) using Fick's first law, assuming a linear concentration gradient (see Supplementary information for calculation). With no electrolyte flow, the boundary layer thickness is greater than 160  $\mu\text{m}$ , a similar length scale to that between the working and counter electrodes, indicating significant concentration polarization. Increasing the flow rate to 2 mL/min decreases the boundary layer to approximately 33  $\mu\text{m}$ , demonstrating improved mass transport to the working electrode. Further increases in flow rate led to more modest reductions in the boundary layer thickness. These thicknesses are smaller than that identified in a recent study of standard protocols for  $\text{CO}_2\text{R}$  catalysis, indicating that the hydrodynamic control in the cell is sufficient to replicate benchmarking conditions. This capability is critical when studying catalytic reactions with *operando* probes, as the significant concentration polarization in static electrolyte makes it challenging to assess the intrinsic reaction kinetics.

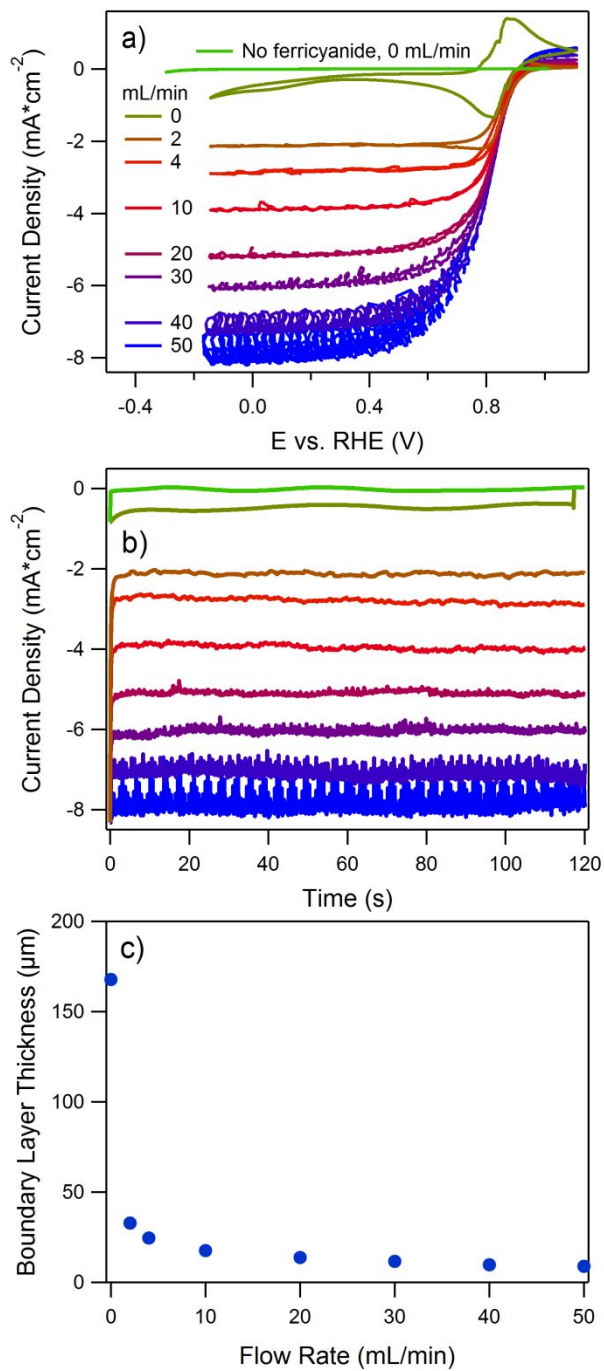


**Figure 2:** a) Cyclic voltammograms for Au electrodes in 0.010 M  $\text{K}_3[\text{Fe}(\text{CN})_6]$ , 0.10 M  $\text{K}_x\text{H}_{3-x}\text{PO}_4$  (pH  $\sim$  6.9) collected at 50 mV/s. b) Steady-state current density measurements for Au electrodes in 0.010 M  $\text{K}_3[\text{Fe}(\text{CN})_6]$ , 0.10 M  $\text{K}_x\text{H}_{3-x}\text{PO}_4$  (pH  $\sim$  6.9) collected at a transport-limited potential of 0 V vs. RHE. c) Boundary layer thickness for ferricyanide reduction as a function of flow rate calculated using Fick's first law. All data was collected using the cell shown in Figure 1.

To assess how the improved hydrodynamics from electrolyte flow affect bubble accumulation, we examined the quality of GIXRD and GIXAS data from Cu thin-film catalysts operating at HER current densities comparable to or exceeding those typically used to evaluate the performance of HER catalysts. Experiments were conducted in an Ar-sparged 0.1 M potassium phosphate buffer with a bulk pH of 6.8, while the Cu thin-film working electrode was held at -1.1 V vs. RHE. Significant HER current densities were observed at an electrolyte flow rate of 45 mL/min (Figure 3a), which is particularly noteworthy as the Cu thin-films are planar and are thus operating at substantial turnover frequencies. An increase in the HER current is seen during the early portion of this experiment before the current stabilizes after  $\sim 4000$  s. Deposition of Pt from the counter electrode onto the Cu sample could lead to an increase in HER current as Pt displays higher intrinsic activity for the HER than Cu does. *Ex situ* XPS and low-energy ion scattering analysis of Cu working electrodes after similar electrolysis suggest that a small amount of Pt deposits on the sample at high current densities (Figures S2 and S3), indicating that the electrolyte flow combined with chelating agents<sup>35</sup> in the electrolyte sparge chamber mitigates but does not completely prevent contamination of the working electrode. However, contamination at such low concentrations is unlikely to have a strong impact on either the GIXRD or GIXAS data, and we are searching for suitable replacement counter electrodes.

*Operando* XRD (Figure 3b), X-ray absorption near edge structure (XANES) (Figure 3c), and extended X-ray absorption fine structure (EXAFS) (Figure 3d) measurements demonstrate that data with a high signal to noise ratio can be collected even at these substantial reaction rates. Taken together, the results demonstrate how

control over the cell hydrodynamics significantly improves *operando* analysis of phenomena at the catalyst-electrolyte interface, enabling the collection of data at a fidelity that was previously impossible at these reaction rates.

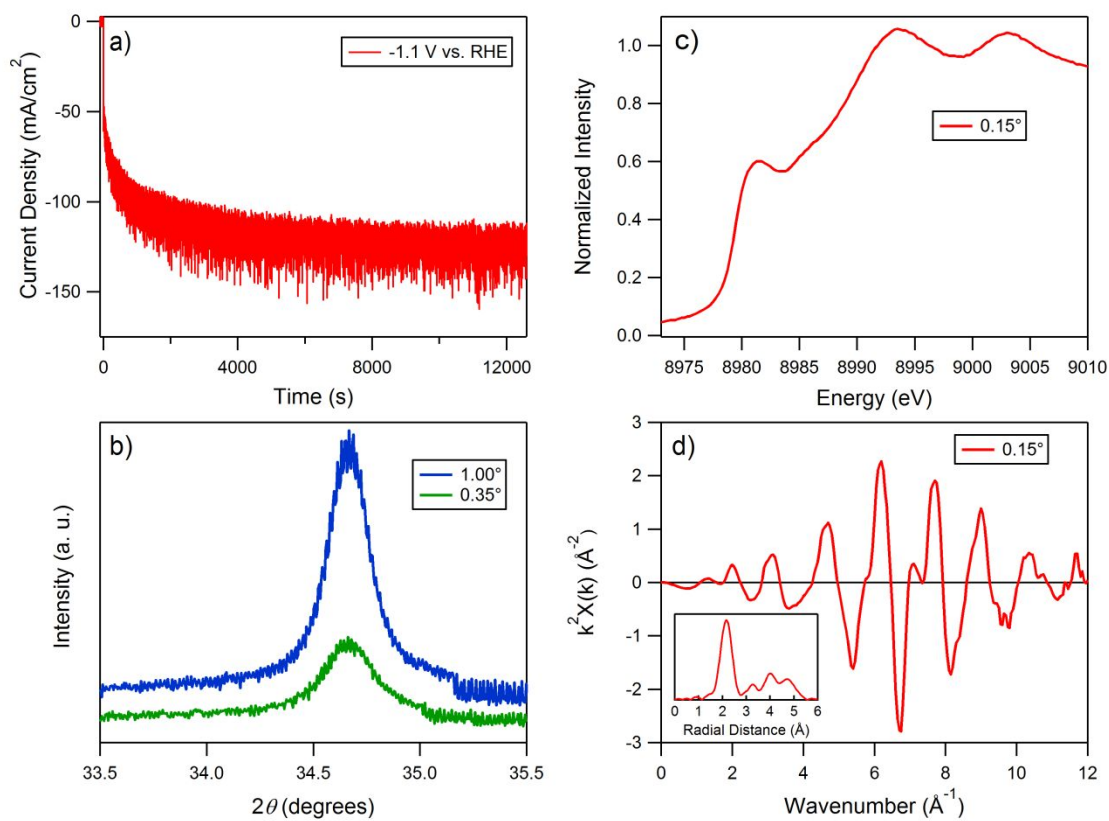


**Figure 3:** a) Current density of a Cu thin film sample operating at -1.1 V vs. RHE in a 0.1 M, pH 6.8 potassium phosphate solution, with an electrolyte flow rate of 45 mL/min. b) XRD of the Cu sample at grazing angles of 1.00° and 0.35°. c) XANES and d) k-space EXAFS ( $k^2$ -weight) with Fourier-transformed EXAFS inset of the Cu sample at 0.15° grazing angle.

### Interfacial Characterization by *Operando* GIXRD and GIXAS

To demonstrate the sensitivity of this combined *operando* GIXAS and GIXRD technique to the chemical and structural evolution of a catalyst surface, we examined the

redox behavior of Cu thin-film surfaces in 0.1 M potassium carbonate, an electrolyte that is relevant to electrochemical CO<sub>2</sub>R. As expected, the GIXAS measurements indicate that the electrode potential controls the preferred oxidation state of the Cu thin film surface. Figure 4a illustrates Cu K-edge XANES spectra of the Cu thin film *ex situ* under dry conditions, *in situ* immersed in electrolyte at the OCP, and *operando* immersed in electrolyte at -0.5 V vs. RHE. The XANES spectrum of the dry Cu thin-film at a grazing-incidence angle of 0.15°, corresponding to a ~2 nm probe depth (Figure S4), shows features of a copper oxide layer on the surface, with metallic copper underneath. The lowered spectral intensity near 8982 eV and increased spectral intensity near 8997 eV indicate a mixture of CuO and metallic Cu, and possibly other oxidized phases, consistent with an oxide layer formed due to air exposure. At the OCP with no electrolyte flow, the XANES spectrum of the surface displays features characteristic of Cu (I). Both the rising edge peak position of 8981.6 eV and the main edge peak at 8996.3 eV match prominent features in the Cu<sub>2</sub>O reference sample.

Since the electrolyte equilibrates to a bulk pH of 10 after Ar-sparging, at the measured open-circuit potential (OCP) of approximately -0.05 V vs. SHE, the Pourbaix diagram Figure S6 indicates that Cu<sub>2</sub>O is thermodynamically favorable. Previous work showed that a smooth and contiguous Cu<sub>2</sub>O layer (~22 nm thick) is formed on top of Cu after immersion in a pH 10 solution for 24 hours. In the present work, we expect that the oxide layer formed from exposure to the electrolyte is thinner than 22 nm, as our Cu thin film was only left at the OCP for ~ 6 hours before changing the electrode potential. The observed edge position of 8994 eV corroborates this conclusion as it matches that of the Cu foil standard, indicating there is only a thin Cu(I) layer that co-exists with metallic

Cu. At a grazing-incidence angle of 11 degrees (bulk), corresponding to a  $\sim 1 \mu\text{m}$  probe depth (Figure S4), the spectrum matches that of the Cu foil standard, suggesting that the Cu(I) layer exists on top of metallic Cu(0).

After applying an electrode potential of  $-0.5 \text{ V}$  vs. RHE, the surface Cu(I) phase is effectively reduced to Cu(0) (Figure 4a). At this reductive potential, the rising edge and main-edge peaks at the surface correspond to those of the Cu foil, suggesting that the surface oxide layer is completely reduced, and that metallic Cu is the active surface at  $-0.5 \text{ V}$  vs. RHE. Differences in spectral intensities between the surface and Cu foil standard are due to angle-dependent self-absorption effects at grazing angles (Figure s6). While applying an electrode potential of  $-0.5 \text{ V}$  vs. RHE, we increased the electrolyte flow rate from 0 to 5 mL/min to mitigate the impacts of concentration polarization and bubbles formed from the HER. A comparison of the difference spectrum for the thin-film surface at the OCP and  $-0.5 \text{ V}$  vs. RHE (sample difference spectrum) to that of the Cu foil and Cu<sub>2</sub>O standards (standard difference spectrum) supports the conclusion that the surface oxide at OCP is predominantly Cu<sub>2</sub>O (Figure 4b). While quantitative linear combination fitting to determine the Cu(I) layer thickness is complicated by the need for rigorous self-absorption corrections, a rough estimate is made by applying a simple correction (see Supplemental Information), followed by scaling the sample difference spectrum by a factor of 3 to match the standard difference spectrum. This indicates that the Cu(I) surface layer contributes  $\sim 1/3$  of the total signal, corresponding to a thickness of  $\sim 1\text{-}2 \text{ nm}$ . Discrepancies between the difference spectra, notably between 8982 and 8990 eV, indicate that the Cu(I) layer differs from crystalline Cu<sub>2</sub>O, possibly due to contributions from other oxidized species with different structures. These results

highlight the sensitivity of GIXAS for distinguishing the chemical composition of complex multi-phase compounds at catalyst-electrolyte interfaces.

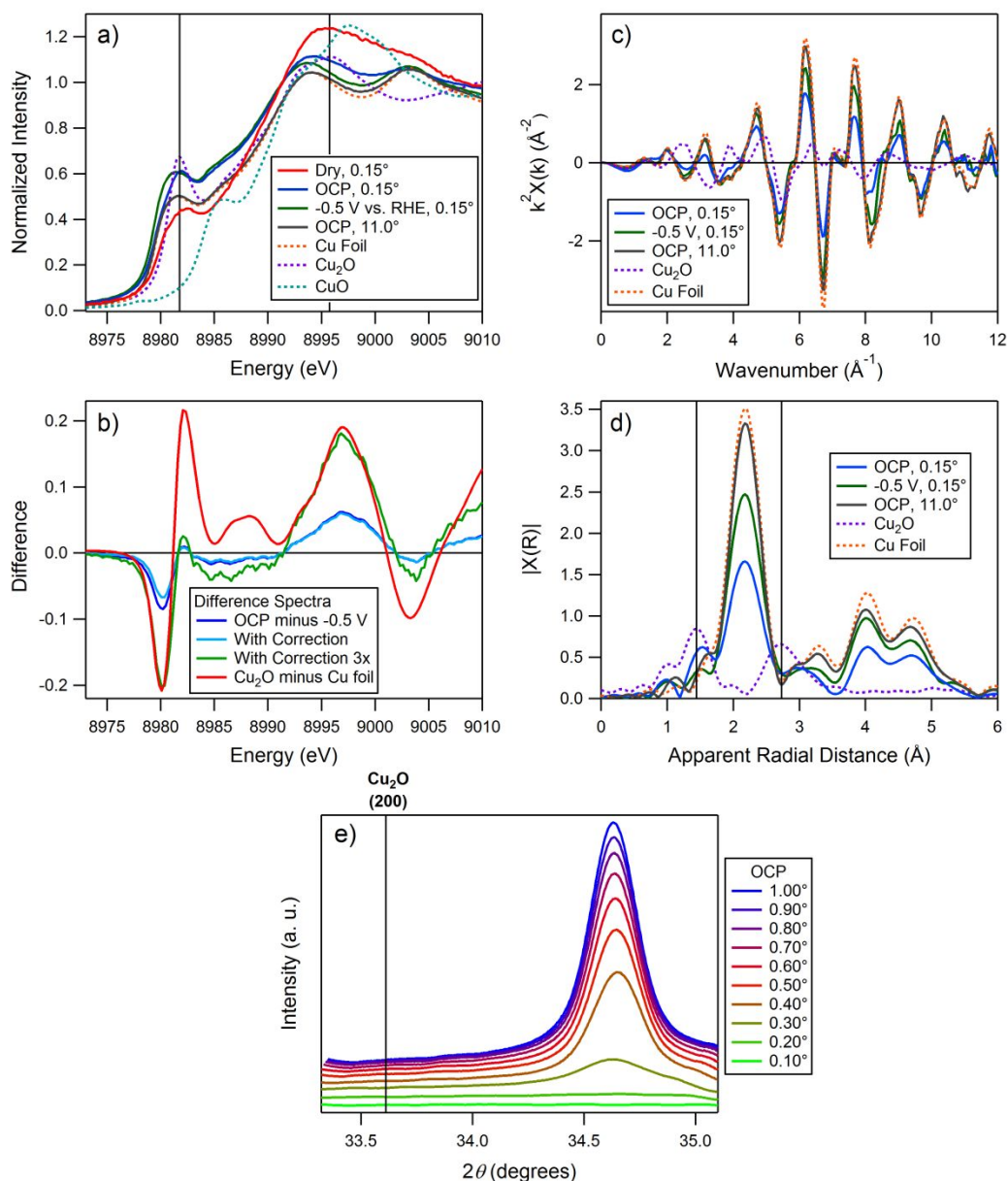


**Figure 4:** a) XANES spectra, b) XANES difference spectra, c) k-space EXAFS spectra, d) Fourier-transformed EXAFS spectra, and e) XRD of the thin-film (100 nm) Cu electrode dry and in pH 10, 0.1 M  $K_xH_{2-x}CO_3$  buffer solution, with comparison to standards. Vertical lines indicate the energy and radial positions of major features in the  $Cu_2O$  reference XANES/EXAFS spectra, and the expected  $Cu_2O$  (200) diffraction peak position in XRD. Potentials are reported vs. RHE.

Complementary to XANES, EXAFS provides information on the local atomic structure in the near surface region. Quantitative analysis is similarly complicated by the need for self-absorption corrections, but the response of the catalyst surface to different potential conditions can be clearly observed. Both the k-space (Figure 4c, k-weight 2) and Fourier transformed (Figure 4d) EXAFS corroborate the existence of a surface Cu(I) layer. At the OCP, the Fourier transformed EXAFS for the Cu thin-film surface (Figure 4d) displays peaks at 1.5 Å and 2.8 Å apparent distance, corresponding to Cu-O and Cu-Cu scattering peaks as seen in the Cu<sub>2</sub>O standard. In addition, there are significant peaks at 2.3 Å and between 3.8 Å and 5 Å that correspond to first and second shell Cu-Cu scattering in metallic Cu, respectively. This is consistent with the XANES spectra, indicating that Cu(I) and Cu(0) co-exist in the region near the surface. As in the XANES, bulk EXAFS closely matches the Cu foil standard, indicating the Cu(I) exists only at the surface. At -0.5 V vs. RHE, the peaks at 1.5 Å and 2.8 Å disappear at the surface, while the large peak at ~ 2.2 Å and the second shell scattering features between 3.8 Å and 5 Å both increase in intensity. This is consistent with the observation that the surface Cu(I) layer has been reduced to Cu(0).

In contrast to GIXAS measurements, grazing-incidence X-ray diffractograms of the identical thin-film surface show no evidence of the existence of Cu<sub>2</sub>O (Figure 4e), suggesting that the oxide is disordered. To determine the feasibility of detecting a relatively disordered oxide layer using XRD, diffractograms were simulated using PowderCell to estimate the intensities of the Cu(111) and Cu<sub>2</sub>O(200) peaks given an oxide:metal ratio of 2:1, as estimated from the XANES difference spectra.<sup>38</sup> Scherrer analysis indicates that the oxide peak must be roughly four times as broad (FWHM) as

that of the metal to not be detected in the XRD measurement (Figure s8), suggesting the mean size of the crystalline Cu(I) domains to be at least four times smaller than the metallic Cu. These results demonstrate some of the advantages of combining GIXAS and GIXRD measurements in the same reaction conditions, as it was necessary to examine both the local atomic environment and long-range order to comprehensively understand the structure of the catalyst surface.

The analysis presented above provides a powerful means to interrogate electrocatalyst surfaces under *operando* conditions, but conclusions could be made more quantitative with rigorous corrections for self-absorption effects in GIXAS, as discussed in the Supplemental Information. New schemes to treat self-absorption effects at grazing incidence must be developed, but they will allow for robust determination of surface layer thicknesses, making *operando* GIXAS an even more powerful tool for understanding electrode-electrolyte interfaces at an atomistic level.

## Conclusion

By developing and implementing an electrochemical flow cell that allows for *operando* GIXAS and GIXRD measurements to be collected under identical HER conditions, we demonstrate that these techniques are powerful tools for studying catalyst-electrolyte interfaces. Electrolyte flow mitigates bubble formation and improves mass transport within the cell, allowing high-quality data to be collected even at current densities in excess of  $-100 \text{ mA/cm}^2$ . We show that these techniques are highly sensitive to chemical and structural changes in the near surface region of a catalyst by studying the *operando* reduction of a Cu(I) surface layer on Cu(0). Spectral features from GIXAS clearly show the conversion of Cu(I) to Cu(0) after reduction, demonstrating the

sensitivity of the method to the chemical state of the surface. The lack of Cu oxide peaks from GIXRD indicates that the oxide is likely disordered, demonstrating the strength of combining observations of the local atomic structure and long-range order to obtain new insights on the redox behavior of Cu thin-film catalysts. By accessing the same conditions to evaluate catalysts, these *operando* probes can connect key fundamental processes at the catalyst surface to performance, enabling the directed design of improved electrocatalytic systems.

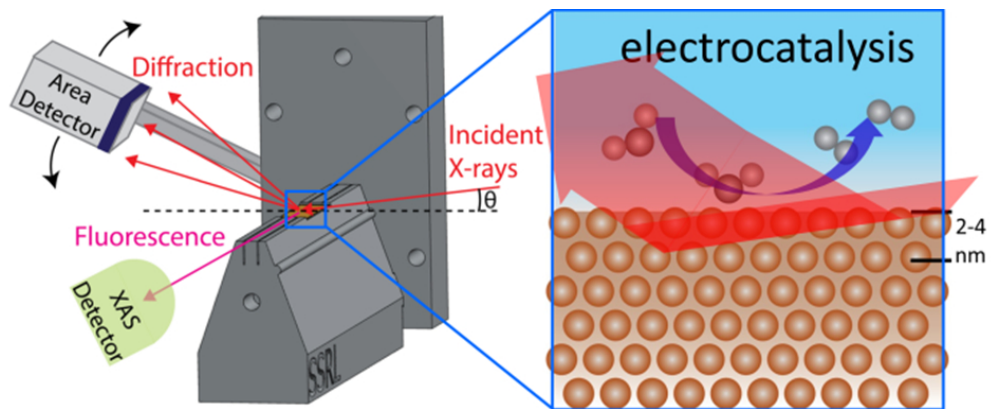
**Acknowledgements**

This material is based on work performed by the Joint Center for Artificial Photosynthesis, a DOE Energy Innovation Hub, supported through the Office of Science of the U.S. Department of Energy, under Award No. DE-SC0004993. Use of the Stanford Synchrotron Radiation Lightsource, SLAC National Accelerator Laboratory, is supported by the U.S. Department of Energy, Office of Science, Office of Basic Energy Sciences under Contract No. DE-AC02-76SF00515. Part of this work was performed at the Stanford Nano Shared Facilities (SNSF) and the Stanford Nanofabrication Facility (SNF), supported by the National Science Foundation under Award ECCS-1542152. We acknowledge Peter Lobaccaro for insightful discussions on cell design. We would also like to thank Charles Troxel, Jr., Cynthia Patty, Samuil Belopolskiy, Valery Borzenets, Risa Benwell, Matthew Padilla, and Cathy Knotts for their support at SSRL.

**References**

1. M. D. Tikekar, S. Choudhury, Z. Tu and L. A. Archer, *Nat. Energy*, 2016, **1**, 16114.
2. A. S. Aricò, P. Bruce, B. Scrosati, J.-M. Tarascon and W. van Schalkwijk, *Nat. Mater.*, 2005, **4**, 366.
3. J. H. Montoya, L. C. Seitz, P. Chakthranont, A. Vojvodic, T. F. Jaramillo and J. K. Nørskov, *Nat. Mater.*, 2016, **16**, 70.
4. K. P. Kuhl, E. R. Cave, D. N. Abram and T. F. Jaramillo, *Energy Environ. Sci.*, 2012, **5**, 7050-7059.
5. P. Mukherjee, A. Lagutchev and D. D. Dlott, *J. Electrochem. Soc.*, 2012, **159**, A244-A252.
6. B. G. Nicolau, N. García-Rey, B. Dryzhakov and D. D. Dlott, *J. Phys. Chem. C*, 2015, **119**, 10227-10233.
7. Z. Zeng, W.-I. Liang, H.-G. Liao, H. L. Xin, Y.-H. Chu and H. Zheng, *Nano Lett.*, 2014, **14**, 1745-1750.
8. Y.-G. Kim, A. Javier, J. H. Baricuatro and M. P. Soriaga, *Electrocatalysis*, 2016, **7**, 391-399.
9. H. Wang, Y.-W. Zhou and W.-B. Cai, *Curr. Opin. Electrochem.*, 2017, **1**, 73-79.
10. M. Osawa, *Bull. Chem. Soc. Jpn.*, 1997, **70**, 2861-2880.
11. A. Wuttig, C. Liu, Q. Peng, M. Yaguchi, C. H. Hendon, K. Motobayashi, S. Ye, M. Osawa and Y. Surendranath, *ACS Central Science*, 2016, **2**, 522-528.
12. I. Oda, H. Ogasawara and M. Ito, *Langmuir*, 1996, **12**, 1094-1097.
13. J. Heyes, M. Dunwell and B. Xu, *J. Phys. Chem. C*, 2016, **120**, 17334-17341.
14. Y.-G. Kim, J. H. Baricuatro, A. Javier, J. M. Gregoire and M. P. Soriaga, *Langmuir*, 2014, **30**, 15053-15056.
15. M. F. Lichterman, S. Hu, M. H. Richter, E. J. Crumlin, S. Axnanda, M. Favaro, W. Drisdell, Z. Hussain, T. Mayer and B. S. Brunshwig, *Energy Environ. Sci.*, 2015, **8**, 2409-2416.
16. M. Favaro, B. Jeong, P. N. Ross, J. Yano, Z. Hussain, Z. Liu and E. J. Crumlin, *Nat. Comm.*, 2016, **7**, 12695.
17. M. Favaro, J. Yang, S. Nappini, E. Magnano, F. M. Toma, E. J. Crumlin, J. Yano and I. D. Sharp, *J. Am. Chem. Soc.*, 2017, **139**, 8960-8970.
18. M. F. Toney, J. G. Gordon, M. G. Samant, G. L. Borges, O. R. Melroy, L.-S. Kau, D. G. Wiesler, D. Yee and L. B. Sorensen, *Phys. Rev. B*, 1990, **42**, 5594-5603.
19. K. M. Robinson and W. E. O'Grady, *J. Electroanal. Chem.*, 1995, **384**, 139-144.
20. F. U. Renner, Y. Gruender and J. Zegenhagen, *Rev. Sci. Instrum.*, 2007, **78**.
21. C.-M. Wang, *J. Mater. Res.*, 2015, **30**, 326-339.
22. B. Lassalle-Kaiser, S. Gul, J. Kern, V. K. Yachandra and J. Yano, *J. Electron Spectrosc. Relat. Phenom.*, 2017, **221**, 18-27.
23. B. M. Ocko, J. Wang, A. Davenport and H. Isaacs, *Phys. Rev. Lett.*, 1990, **65**, 1466-1469.
24. N. J. Firet, M. A. Blommaert, T. Burdyny, A. Venugopal, D. Bohra, A. Longo and W. A. Smith, *J. Mater. Chem. A*, 2019, **7**, 2597-2607.
25. P. Grosse, D. Gao, F. Scholten, I. Sinev, H. Mistry and B. R. Cuenya, *Angew. Chem.*, 2018, **130**, 6300-6305.
26. Y. Deng and B. S. Yeo, *ACS Catal.*, 2017, **7**, 7873-7889.

27. N. Hodnik, G. Dehm and K. J. J. Mayrhofer, *Acc. Chem. Res.*, 2016, **49**, 2015-2022.
28. E. L. Clark, J. Resasco, A. Landers, J. Lin, L.-T. Chung, A. Walton, C. Hahn, T. F. Jaramillo and A. T. Bell, *ACS Catal.*, 2018, **8**, 6560-6570.
29. C. C. L. McCrory, S. Jung, I. M. Ferrer, S. M. Chatman, J. C. Peters and T. F. Jaramillo, *J. Am. Chem. Soc.*, 2015, **137**, 4347-4357.
30. B. L. Henke, E. M. Gullikson and J. C. Davis, *Atomic Data and Nuclear Data Tables*, 1993, **54**, 181-342.
31. S. Reither, W. Artner, A. Eder, S. Larisegger, M. Nelhiebel, C. Eisenmenger-Sittner and G. Fafilek, In-Situ Gracing Incidence X-Ray Diffraction Cell for Electrochemically Formed Thin Films, 2017.
32. M. Ndjeri, S. Peulon, M. L. Schlegel and A. Chaussé, *Electrochem. Commun.*, 2011, **13**, 491-494.
33. M. Escudero-Escribano, A. F. Pedersen, E. T. Ulrikkeholm, K. D. Jensen, M. H. Hansen, J. Rossmeisl, I. E. L. Stephens and I. Chorkendorff, *Chem. Eur. J.*, 2018, **24**, 12280-12290.
34. T. A. Petach, M. Lee, R. C. Davis, A. Mehta and D. Goldhaber-Gordon, *Phys. Rev. B*, 2014, **90**, 081108.
35. A. Wuttig and Y. Surendranath, *ACS Catalysis*, 2015, **5**, 4479-4484.
36. M. Pourbaix, *Atlas of Electrochemical Equilibria in Aqueous Solutions*, National Academy of Corrosion Engineers, Houston, Texas, 1974.
37. Y. Feng, K.-S. Siow, W.-K. Teo, K.-L. Tan and A.-K. Hsieh, *Corrosion*, 1997, **53**, 389-398.
38. W. Kraus and G. Nolze, *J. Appl. Crystallogr.*, 1996, **29**, 301-303.



79x32mm (300 x 300 DPI)